ELSEVIER

Dead-ended anode polymer electrolyte fuel cell stack operation investigated using electrochemical impedance spectroscopy, off-gas analysis and thermal imaging

CrossMark

Quentin Meyer [a], Sean Ashton [b], Oliver Curnick [b], Tobias Reisch [b], Paul Adcock [b], Krisztian Ronaszegi [a], James B. Robinson [a], Daniel J.L. Brett [a,*]

[a] Electrochemical Innovation Lab, Department of Chemical Engineering, UCL, London WC1E 7JE, United Kingdom
[b] Intelligent Energy, Charnwood Building, Holywell Park, Ashby Road, Loughborough, Leicestershire LE11 3GB, United Kingdom

HIGHLIGHTS

- Dynamics of anode dead-end/purge operation investigated.
- Reconstructive impedance allows complete spectra with high temporal resolution.
- Water build-up and N_2 cross-over cause performance loss in dead-end mode.

GRAPHICAL ABSTRACT
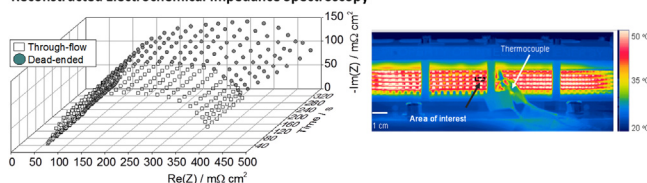
ARTICLE INFO

ABSTRACT

Dead-ended anode operation, with intermittent purge, is increasingly being used in polymer electrolyte fuel cells as it simplifies the mass flow control of feed and improves fuel efficiency. However, performance is affected through a reduction in voltage during dead-ended operation, particularly at high current density. This study uses electrochemical impedance spectroscopy (EIS), off-gas analysis and high resolution thermal imaging to examine the source of performance decay during dead-ended operation. A novel, 'reconstructed impedance' technique is applied to acquire complete EIS spectra with a temporal resolution that allows the dynamics of cell processes to be studied.

The results provide evidence that upon entering dead-ended operation, there is an initial increase in performance associated with an increase in anode compartment pressure and improved hydration of the membrane electrolyte. Subsequent reduction in performance is associated with an increase in mass transport losses due to a combination of water management issues and build-up of N_2 in the anode. The purge process rapidly recovers performance. Understanding of the processes involved in the dead-end/purge cycle provides a rationale for determining the optimum cycle frequency and duration as a function of current density.

© 2013 Elsevier B.V. All rights reserved.

1. Introduction

Polymer electrolyte fuel cells (PEFCs) operating on hydrogen offer the possibility of zero-emission electricity generation. The technology has shown significant advances in terms of performance and durability, and wide-scale commercialisation in a range of applications is imminent.

Within the broad category of PEFCs a range of design variants and operational modes exist. Dead-ended anode operation is a common mode as it can simplify the system, potentially avoiding flow meters and humidifiers. The configuration typically employs a single pressure regulator before the hydrogen inlet to the stack and a purge valve after the anode outlet [1]. However, dead-ended
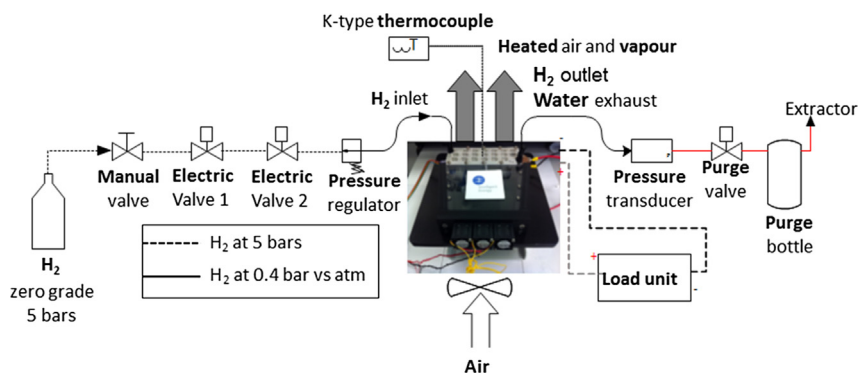
Fig. 1. Illustration of the system test rig.

anode operation leads to a gradual voltage loss. Therefore, a purge valve is intermittently opened at regular intervals, leading to instantaneous recovery of cell voltage(s).

The gradual voltage loss has been measured and modelled [2–6], highlighting the influence of several factors. Nitrogen cross-over from the cathode to the anode, across the Nafion membrane, has been reported to have a significant influence [4,7,8]. This has been confirmed by controlling the nitrogen-to-hydrogen ratio at the anode inlet [9]. The extent of N_2 cross-over from cathode to anode (the permeation factor) is of particular relevance for dead-ended operation and has been shown to increase with increasing current density and temperature [7,10]. Similarly, water back-diffusion (cathode to anode) has been studied using neutron imaging before and after anodic purge [11] and found to increase with increasing current density [12]. The effect of dead-ended operation on degradation processes has been investigated [9,13] along with the effect of carbon corrosion in this mode of operation [14]. However, without a clear understanding of what is happening during dead-end/purge processes it is difficult to reconcile the cause of degradation, and take measures to avoid it.

Monitoring temperature transients and distribution in fuel cells is a useful way to study their operation [15], and offers potential insight into the dead-end/purge process. Thermocouples can provide a crude measure of temperature inside fuel cells [16–19] but have accuracy limited to ± 1 °C and cannot easily provide high spatial resolution. Moreover, thermocouples need to be inserted inside the fuel cell, which often requires modifications of design. Alternatively, thermal imaging can provide very high spatial and temperature resolution [15,20–25]. Here, a thermal imaging camera is used to perform localised measurements on an air cooled stack to characterise heat generation, and dissipation, in the stack.

Electrochemical impedance spectroscopy (EIS) is an established and powerful tool for fuel cell characterisation [26–28], providing insightful information on the various resistive losses occurring in operational fuel cells. EIS has been used to characterise PEFC response to CO poisoning [29], decouple anode and cathode operation [30], and the effect of specific components (e.g. platinum loading, membrane thickness, GDL structure) [26]. EIS has also found applications in distributed localized measurements [31,32], fault detection and flooding/drying events [33,34].

However, EIS has not been used for dead-end/purge analysis due to the challenge of capturing the process on the relatively short duration of the purge event. The present work uses single-frequency high-frequency impedance measurements, along with a novel 'reconstructed impedance' method that combines the result of consecutive repeatable cycles to build up full EIS during through-flow/dead-ended operation.

2. Experimental

2.1. Test station operation

Fuel cell stack operation was carried out using a 5-cell, 60 cm^2 active area electrode, air-cooled open-cathode stack (Intelligent Energy Ltd., UK). The membrane electrode assembly is composed of commercially available gas diffusion layers and commercially available state-of-the art membrane with Pt loading of 0.1 and 0.4 mg cm^{-2} on the anode and cathode, respectively.

This test system (Fig. 1) supplies dry, non-heated, hydrogen (with a purity of 99.995%) into the anodes and air is blown by three fans to the active cathodes and cooling channels (Fig. 2). The fans, which provide cooling and air supply to the cathode, are controlled by a programmable power supply (3649A Agilent). The fans maintain the stack's temperature between 20 and 50 °C with PID controllers. The fuel cell is electrically loaded using a commercial programmable load (Agilent 6060B). An in-house computer controlled system coordinates the air, hydrogen, cooling and electrical valves (LabVIEW, National Instruments). Through-flow and dead-ended operations were achieved by having the purge valve opened and closed, respectively. Ambient temperature, pressure
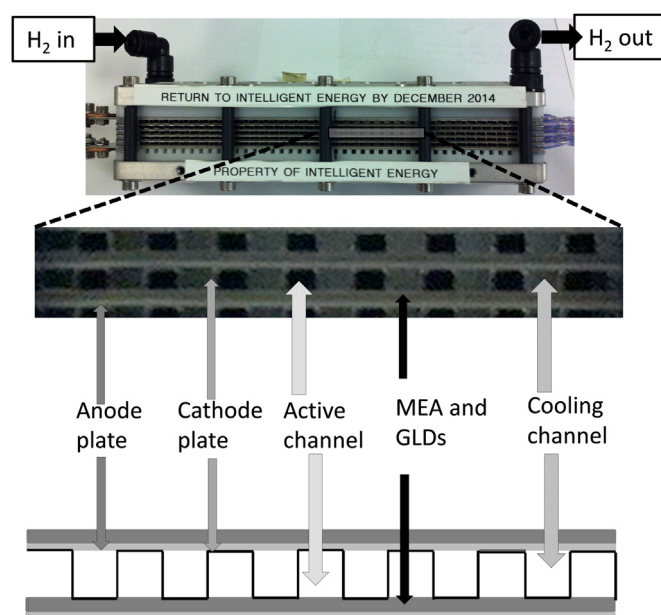

Fig. 2. Picture and simplified scheme of the fuel cell stack showing 'active' and 'cooling' channels. MEA: membrane electrode assembly. GDL: gas diffusion layer.
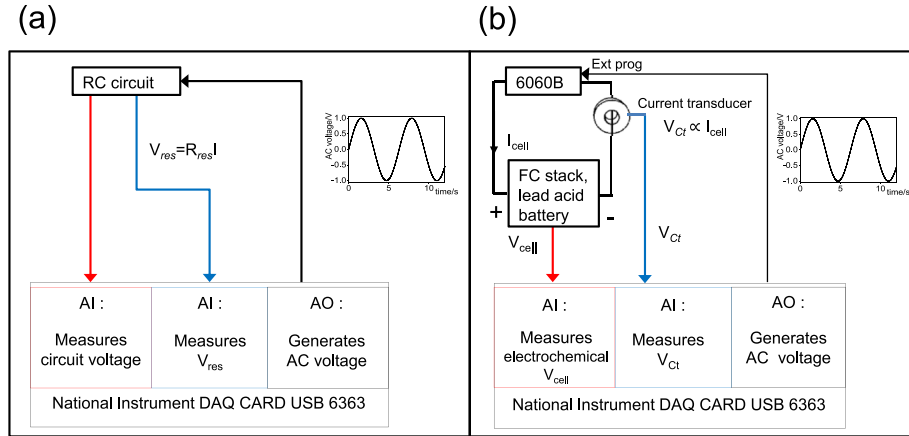
(a)   (b)

Fig. 3. UCL-FRA for impedance spectroscopy on: (a) passive systems and (b) active electrical power generation systems. AI: analog input; AO: analog output.

(absolute) and room humidity (RH) were measured, being of around 25 °C, 40% RH and 1.02 bar respectively, during all tests. The exhaust hydrogen flow rate in through-flow mode was measured using a thermal flow meter (MassVIEW, Bronkhorst) to be 2 SLPM.

2.2. Temperature measurements

A K-type thermocouple was inserted into the central cooling channel of the third cell (middle cell) for temperature control of the stack. Thermal imaging was performed using a 640 × 512 focal plane array camera (SC5600MB FLIR, UK). The images were recorded using commercially available software (ResearchIR, FLIR ATC, Croissy-Beaubourg, France). The camera has an extended wavelength detector allowing detection of infrared light within the range 2.5 μm–7 μm. For the purposes of this experiment the calibration was limited to temperatures ranging from 5 to 85 °C using 4 integration times. The cavity nature of the cooling and active channels approximate to quasi-blackbody emitters, allowing an emissivity of 1 to be used during calculations. The thermal camera used during the experiments has a noise equivalent temperature difference (NETD), a measure of the signal-to-noise ratio, of approximately 19 mK which is within the range of calibration required for the accurate measurement of absolute temperatures. The geometry of the systems imaged resulted in a pixel resolution of approximately 27 μm across the image.

2.3. Off-gas analysis

The relative hydrogen and nitrogen concentrations were measured using an ion source mass spectrometer (Prolab Benchtop Fisher Scientific). The mass spectrometer is capable of detecting concentrations of gases down to 10 ppm. The mass spectrometer samples a small stream from the anode, being connected between the hydrogen exhaust and the purge valve, and determines the concentration ratio of the gas flow. The flow to the mass spectrometer was lowered from 1.45 bar to 1 bar using a pressure regulator (Swagelok). The flow to the mass spectrometer is 30 cm^3 min^{-1}, with a pressure drop of 10 mbar, ensuring pseudo dead-ended anode operations during sampling, given that the anode pressure and H$_2$ consumption rate operations are much larger (typically of the order of 400 mbar and 2 SLPM respectively).

2.4. Electrochemical impedance spectroscopy

EIS was performed using a LabVIEW-based frequency response analyser (UCL-FRA) developed in-house and described previously [35]. The system uses a data acquisition (DAQ) card to generate an AC signal. The two operation modes of the UCL-FRA are summarised in Fig. 3, showing it can be applied to passive circuits as well as active systems using an electronic load bank (Agilent 6060B). EIS on fuel cells was recorded between 5 kHz and 1 Hz, due to load limitations above 5 kHz [35] where the load starts to generate a small internal phase shift. AC modulation amplitude was kept at 5% of the DC input signal.

3. Results and discussion

3.1. Voltage losses in through-flow and dead-ended modes

Dead-ended studies were performed by having the purge valve opened briefly at the beginning of each period of dead-ended operation [2,3,36]. In order to investigate the effect of dead-ended/purge cycling under different load conditions a polarisation was performed with steps of 0.083 A cm^{-2} every 5 min, with a purge period of 1 s every 59 s (Fig. 4(a)).

It can be seen that the recoverable voltage drop is not discernible below ∼0.45 A cm^{-2}, but becomes progressively more significant at higher current densities. The increased voltage loss, for a constant purge time, may be attributed to the increased back-diffusion of water from the cathode to the anode, due to higher current densities [12]. It has also been reported that the nitrogen permeation factor and crossover rate increase linearly with the current density [7,10].

In further tests, in order to isolate the through-flow behaviour, the valve was left alternately opened and closed for periods of 180 s. All subsequent tests were performed at 0.75 A cm^{-2}.

It can be seen (Fig. 4(b)) that the voltage of each cell drops at a rate of ∼50 μV s^{-1} in through-flow mode, gradually settling after ∼90 s. In dead-ended mode, each cell undergoes an initial improvement for the first ∼35 s, followed by a drop, with a change of slope from 175 μV s^{-1}–250 μV s^{-1} after ∼80 s. It can be seen that there is a rapid increase in cell pressure on entering dead-ended mode of ∼400 mbar. The initial increase in dead-ended voltage may be associated with the increase in anode H$_2$ pressure, according to Nernstian considerations, Equation (1): an increase of 400 mbar (40,000 Pa) in the hydrogen pressure would correspond to an increase in voltage of 5 mV. This is consistent with the small increase in voltage observed here when first transitioning to dead-ended operation.

$$E = E_o + \frac{RT}{nF} \ln \left(\frac{P_{H_2} P_{O_2}^{\frac{1}{2}}}{P_{H_2O}} \right) \tag{1}$$
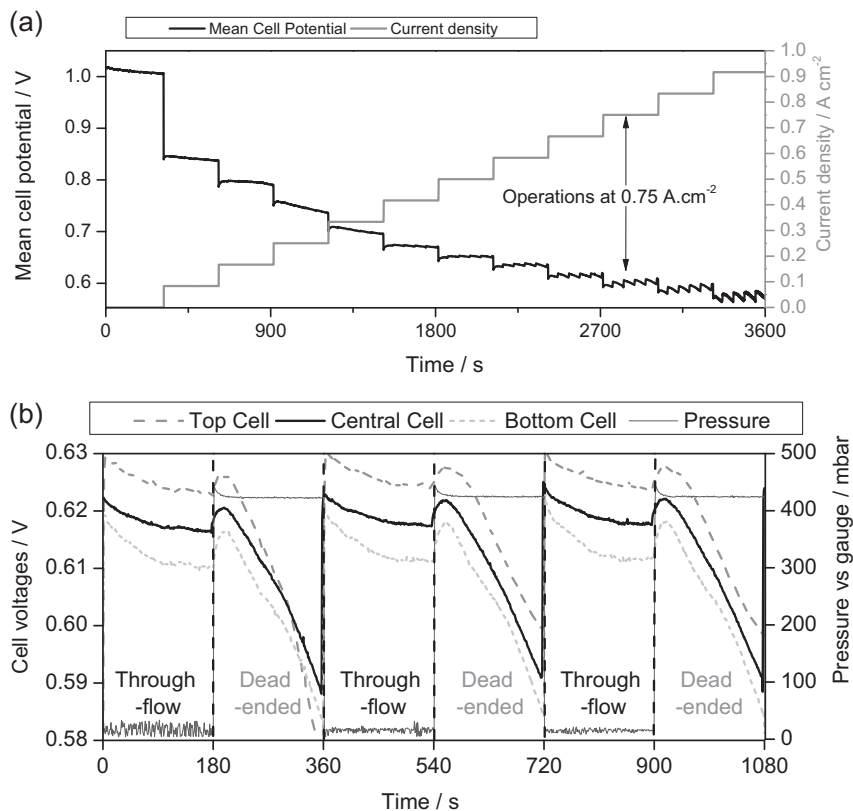
Fig. 4. (a) Effect of dead-end/purge cycling on voltage losses as a function of current density. Current steps of 0.083 A cm^{-2} every 5 min, with a purge period of 1 s every 59 s. (b) Voltage transients and exhaust pressure in through-flow and dead-ended modes for the top, central and bottom cells over a period of 1080 s.

Cell 3, the central cell, is taken as the representative cell in the stack for further studies.

3.2. Off-gas analysis

The off-gas analysis (Fig. 5), confirms published research that accumulation of nitrogen cross-over on the anode occurs during dead-ended operation [4,7–9]. The N$_2$ detected at the anode increases to 3% after 180 s, and reduces back to 0.25% within 30 s in through-flow mode. As the nitrogen ratio increases, the voltage drops. The N$_2$-to-H$_2$ ratio in through-flow eventually becomes stable at 0.25% because the N$_2$ is constantly permeating to the anode but not accumulating there.

For the first 80 s in dead-ended mode there is a slight increase of the nitrogen ratio (0.25%–0.5%) detected at the exit of the stack, this is assumed to be linked to the dead volume of the anode compartment and the aspiration rate of the mass spectrometer causing a lag in the time it takes for the N$_2$ to be detected. There is a similar delay when the system is turned to through-flow.

Then, over the next 100 s, the nitrogen ratio increases from 0.5% to 3%. Nitrogen diffuses at a constant crossover rate (at constant current, and pressure), leading to a decreased hydrogen partial pressure on the anode.

Another possible explanation for the linear accumulation of nitrogen in the anodic compartment is that be that BOC 'zero grade' hydrogen contains roughly 50 ppm nitrogen. The increase in partial pressure of nitrogen is therefore proportional to the hydrogen usage at 0.75 A cm^{-2}. Considering that each of the 5 cells have an anodic compartment of 1 cm^3, the nitrogen ratio over 180 s will reach 2.3%, which is very close to the values of Fig. 5.

Once the nitrogen starts to accumulate, it affects the voltage and causes a steeper voltage drop from 175 μV s^{-1}–225 μV s^{-1}.

The small increase in N$_2$ detected in the anode off-gas corresponds to a negligible decrease in voltage according to Nernstian considerations (Equation (1)) (an increase of 3% in N$_2$ corresponds to $\sim$0.5 mV decrease in voltage). However, the flux of N$_2$ through the membrane means that there will be a higher concentration at the electrode surface (where the anode potential is defined). Interestingly, reports have shown that similar voltage drops were obtained (from 0.71 V to 0.68 V at 5 bars, and 0.5 A cm^{-2}) when the H$_2$/N$_2$ inlet ratio was altered from 99.999% to 99.2% [9], suggesting that the N$_2$ dilution effect is due to more than simple Nernstian considerations.

Accurate measurement of the water cross-over to the anode is not available using this mass spectrometry method, as the composition in the anode is two-phase and any additional water cross-over is likely to be in the liquid phase. However, it is likely that anode flooding makes a significant cause of voltage drop, this display itself as an increase in mass transport losses, as discernible using EIS (described later).

3.3. Thermal imaging characterisation

The open-cathode configuration enables direct measurement of the temperature of the plates, corresponding to the heat generated in the MEA. Fig. 6 summarises the thermal characteristics of the stack. Fig. 6(a) shows the polarisation of the stack and temperature change (recorded using the control thermocouple). It can be seen that the stack temperature increases linearly with current density, upon start-up from ambient conditions up to $\sim$50 °C, at which the PID controlled air cooling is initiated.

The temperature profile at 0.75 A cm^{-2} (Fig. 6(b)) displays a relatively uniform temperature distribution, with the cooling channels at a consistently lower temperature ($\sim$0.5 °C) than the active channels.
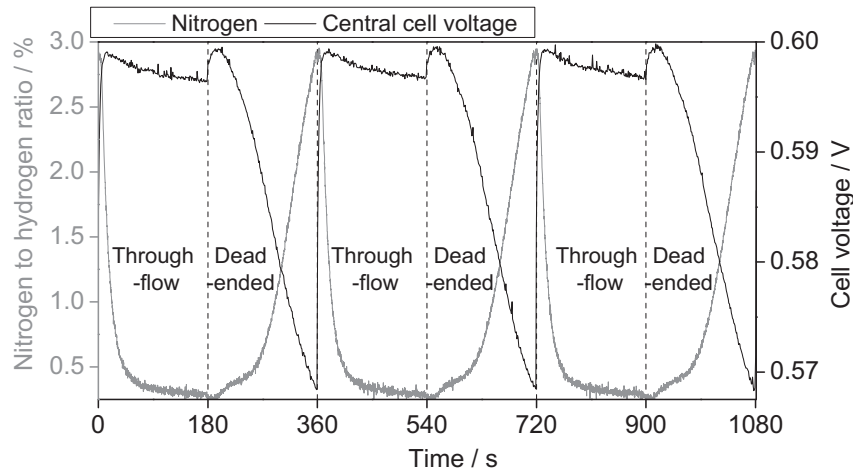
Fig. 5. Voltage transients and exhaust N_2-to-H_2 ratio in through-flow and dead-ended modes for the central cell over a period of 1080 s at 0.75 A cm^{-2}.

The results of Fig. 6(c) are obtained by processing the data from the thermal imaging camera in the central cell at the end of the second quadrant in an active channel and a cooling channel. The system was maintained in through-flow operation for an hour prior to these measurements, to ensure that the temperature and voltage had reached equilibrium.

In Fig. 6(c), the temperature transient from the thermal imaging camera is indicative of the heat transfer from the MEA into the active channel and the cooling channel (see Fig. 2). Both follow the same trend, although the active channel is consistently higher in temperature.

Two distinct behaviours can be seen for the temperature transients. In direct correlation with the voltage response, when transitioning to dead-ended mode the voltage first increases, accompanied by a drop in temperature, this is followed by an increase in temperature with the subsequent drop in voltage.

As described above, on transitioning to dead-ended operation an increase in voltage is observed virtue of the increased pressure, this represents a reduction in heat generated for the constant current maintained. In dead-ended mode the humidity level in the anode compartment will increase, since there is no exhaust water removal. During the first 35 s a favourable humidity level is maintained; however, the humidity level inside the anode compartment will subsequently saturate, flooding the cell, reducing the voltage, which is manifest by the heating effect observed. The temperature evolution is also an indication of localised high current densities, which is a well-known feature occurring during dead-ended operation [13].

3.4. Electrochemical impedance spectroscopy characterisation

3.4.1. Multi-channel EIS

The efficacy of the UCL-FRA multichannel impedance system [35] was first demonstrated by assessing the performance on passive electrical circuits (mode described in Fig. 3(a)). Fig. 7 shows the simultaneous EIS results on a known electrical circuit.

These results show identical plots, with no phase shift between each channel, which demonstrates that the system does not introduce artefacts over the frequency range of interest.

Fig. 8 shows the polarisation (a) and EIS (b) response of the central cell in the stack over a range of current densities up to 1 A cm^{-2}. The arc decreases rapidly in the low current density region (from 0 to 0.3 A cm^{-2}), where the charge transfer is predominant. At higher current density (from 0.5 to 1 A cm^{-2}),
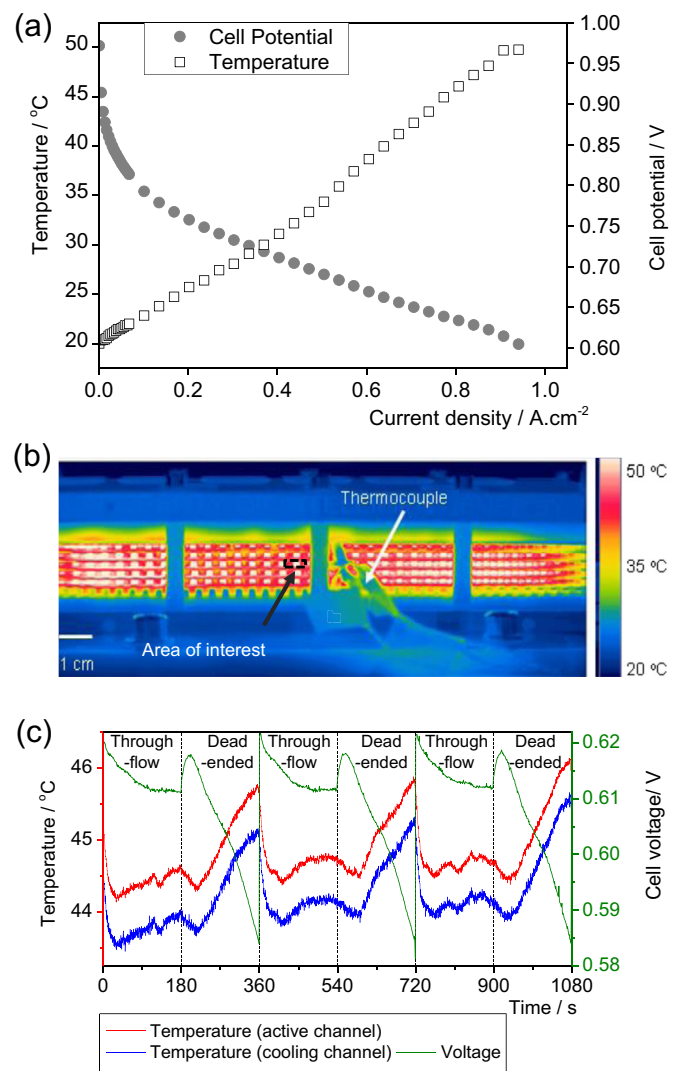

Fig. 6. Temperature evolution and profile of the fuel cell. (a) Evolution of the voltage and temperature between 0 and 1 A cm^{-2}, holding the current constant for 120 s before each measurement; (b) temperature profile at 0.75 A cm^{-2} showing thermocouple placement and channel measurement points; (c) temperature and voltage transients in dead-ended and through-flow modes over a period of 1080 s.

evidence of mass transport begins to show with the emergence of a second lower frequency arc, as described in the literature [37–39].

Fig. 8(c) shows the response of three cells (top, central and bottom) in multichannel mode, at 0.75 A cm^{-2}. The Nyquist plots show slight differences, virtue of location in the stack; however, each displays the same form. Although the features are not fully resolvable, at least two arcs can be discerned, with the low frequency arc associated with mass transport and the higher frequency arc the charge transfer at the cathode.

3.4.2. High frequency resistance

Dead-ended operation is expected to mainly affect the performance of the anode and electrolyte, although the cathode may also be affected indirectly. In order to study the effect of changes in humidity level on the electrolyte, the high-frequency intercept with the real axis (∼2.3 kHz) was considered over the course of the different flow modes.

The transients of the real component observed Fig. 9(c) are relatively small; however, they are highly repeatable. The drop of
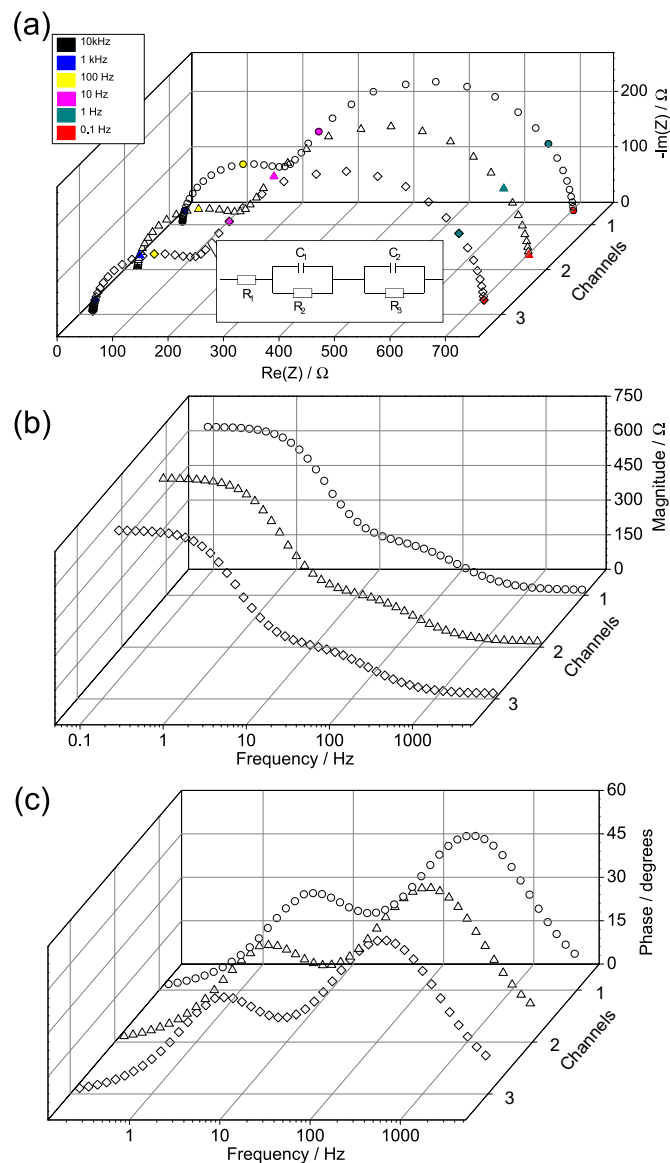
the resistance corresponds to an increase of the conductivity of the membrane, as the hydration level increased by closing the purge valve. After the initial drop, for the first 80 s the resistance is stable.

It increases again after for the next 100 s, which could be indication of possible water saturation, reducing the conductivity between the plate and the gas diffusion layer, increasing the resistance. On the other hand, in through-flow mode, the resistance gradually increases, and settles after ∼100 s, as the membrane dries, due to high flow of hydrogen (2 SLPM).

It should be noted that there may be a large spatial variation of local current during dead-ended operation. Since the high-frequency resistance indicates the overall cell resistance, the specific local conditions are unknown. Local current density could be much higher than the average, and the overall effect could be a drying of the membrane due to the enhanced reaction heat. Localised impedance measurements are therefore desirable for analysing such performance.

3.4.3. Reconstructed EIS

One of the major limitations of the EIS technique (using the conventional single sine method) is that there is a limit on the lowest frequency measurement that can be made, depending on the dynamics of the process. One of the criteria for robust EIS measurement is that the system should be stable and linear [40]. If this is not the case, artifacts can appear in the EIS data as a result of the system changing state over the course of the measurement. For example, a 1 kHz measurement takes 1 ms to collect (assuming that only a single cycle is recorded), which means that rapidly changing processes can be studied with relative accuracy. However, a 0.01 Hz measurement will take 100 s for a single cycle and therefore requires stability over a much longer period. For a full EIS scan, composed of many frequency measurements over several decades, the measurement duration becomes so long that only steady-state systems can be studied. One compromise is to reduce the number of frequencies in the scan; however, this limits the ability to accurately fit equivalent circuits and deconvolute the various processes occurring.

In the case of the dead-ended/through-flow transients observed here, the maximum voltage decay is of the order of 250 μV s^{-1} over a period of 180 s. A full EIS run from 1 kHz to 1 Hz will take ∼220 s using UCL-FRA (each frequency in 7 s, with 10 frequencies per decade). Far too long for the period of the transient or the rate of change of voltage with time.

However, as the dead-ended and purge processes are highly repeatable (as shown in Fig. 4(b)), it is possible to take a measurement of a different frequency during each repeat. In which case each frequency measurement is equivalent to a voltage change of only 1.75 mV and considered pseudo-steady state. The same frequency of interest was measured every 20 s in through-flow and dead-ended conditions, as highlighted in Fig. 10(a). The events were repeated, but changing the frequency of interest (1 kHz–1 Hz) at each repeat. This process took 6 h repeating the through-flow/dead-ended process for 27 frequencies, therefore 27 times, in order to capture frequencies from 1 kHz to 1 Hz.

This novel technique provides seventeen 'reconstructed' Nyquist plots, each of them associated with a different point in the voltage transient, as described in Fig. 10(a). In through-flow mode the EIS response remains relatively unchanged, in dead-ended mode the main arc gradually increases with time. It is not possible to deconvolute the electrode kinetic losses from the mass transport, since increases of resistance can be seen from 100 Hz to 1 Hz.

The robustness of this new impedance technique was challenged by comparing the result with a conventional measurement and applying Kramers–Kronig (K–K) analysis. Fig. 11(a) shows the
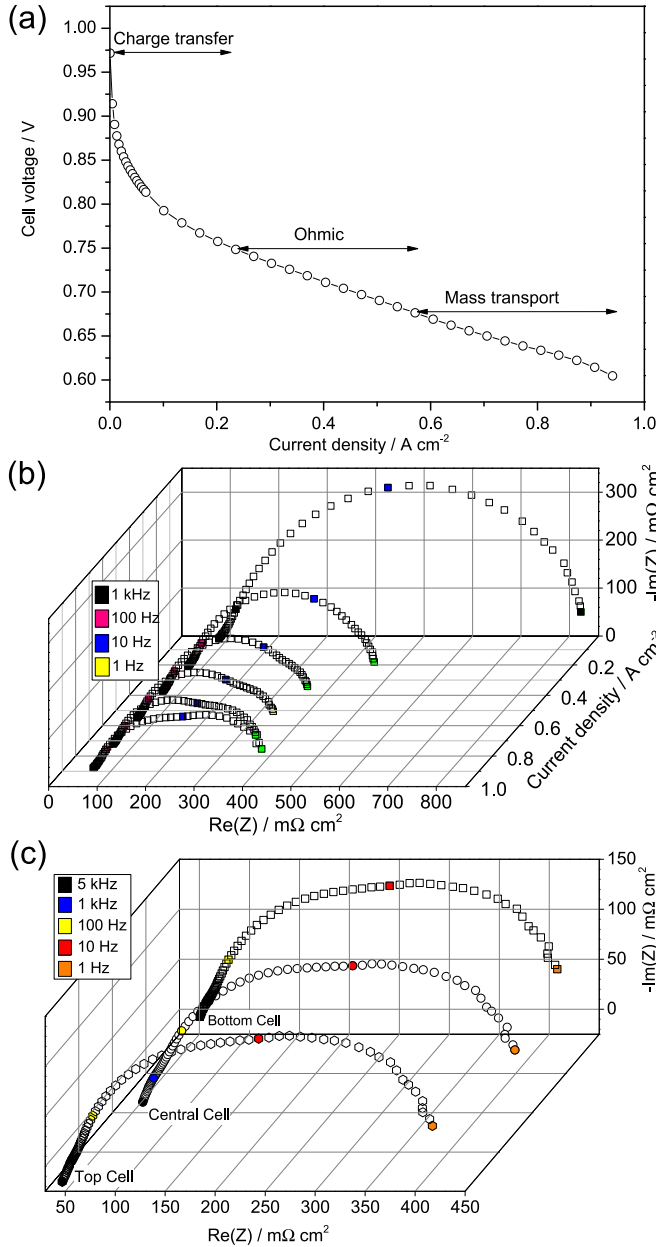

Fig. 7. Simultaneous EIS measurements from three channels on a known electrical circuit. (a) Nyquist plots of the EIS response with electrical circuit inset; (b) magnitude response and (c) phase response.

(a)

(b)

(c)

Fig. 8. (a) Polarisation of the central cell between 0 and 1 A cm^{-2}; (b) EIS measurements of the central cell between 0 and 1 A cm^{-2}, and (c) simultaneous impedance measurements at 0.75 A cm^{-2} on the Top, Central and Bottom cell in through-flow mode.

reconstructed Nyquist plot compared to one collected using a conventional technique in through-flow mode. These two diagrams are seen to be in good agreement.

The K−K relations are used to demonstrate that the electrochemical system responds linearly to the ac perturbation, and that the response of the system cannot precede the perturbation [41–43]. This validation is particularly relevant here since the measurements are performed under dynamic conditions. The K−K transform was performed with a discrete integration between 1 kHz and 1 Hz, using the simulation software developed by Ramanathan [44]. As displayed in Fig. 11(b) and (c), the K−K transforms of the real and imaginary components are nearly identical to the actual real and imaginary. The K−K method therefore supports the validity of the measurement over the frequency range of interest.
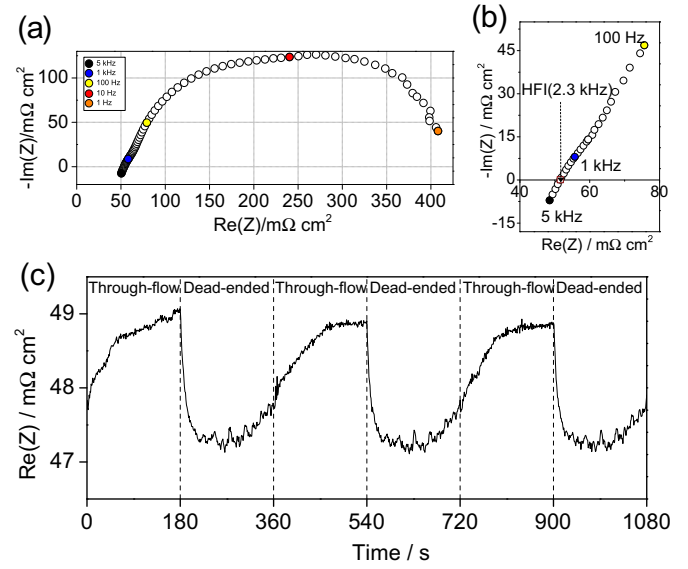
(a)

(b)

(c)

Fig. 9. (a) Detailed Nyquist plot (20 points per decades) at 0.75 A cm^{-2}; (b) high frequency intercept (HFI) with the real axis; and (c) evolution of the real impedance transients in dead-ended and through-flow modes over a period of 1080 s at 2.3 kHz.

It is clear that the complex plane representation in Fig. 10(b) is composed of more than one time constant; however, it is not significantly resolved to allow robust fitting to an equivalent circuit. Rather, a comparison is made between the evolution of the relative magnitude, Equation (2), and phase, Equation (3), in Fig. 12. The relative phase and magnitude in through-flow provides a baseline, changes are only observed under dead-ended conditions.

$$\text{Relative magnitude}(t) = \frac{\text{Magnitude}(t) - \text{Magnitude}(0)}{\text{Magnitude}(0)} \quad (2)$$
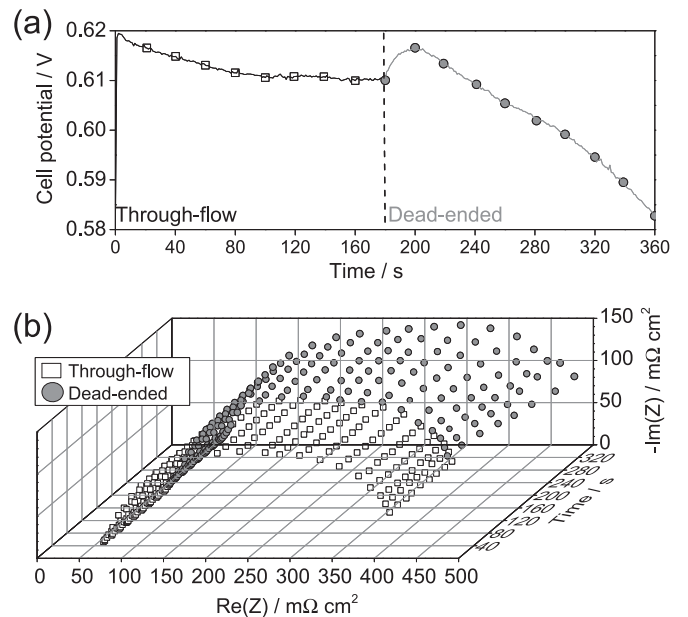
(a)

(b)

Fig. 10. (a) Points under investigation for the reconstructed impedance study at 0.75 A cm^{-2}; (b) reconstructed impedance plots at 0.75 A cm^{-2} over 180 s in through-flow and 180 s in dead-ended operation from 1 kHz to 1 Hz.
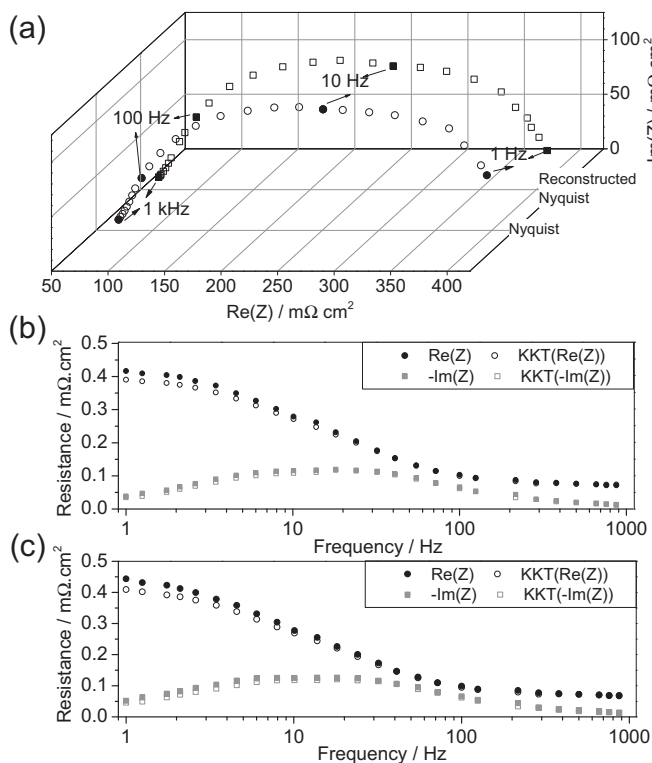
Fig. 11. (a) Reconstructed and conventionally measured Nyquist plots in through-flow mode at 0.75 A cm^{-2}. (b and c) Real, imaginary, and K−K transforms in through-flow and dead-ended modes, respectively.
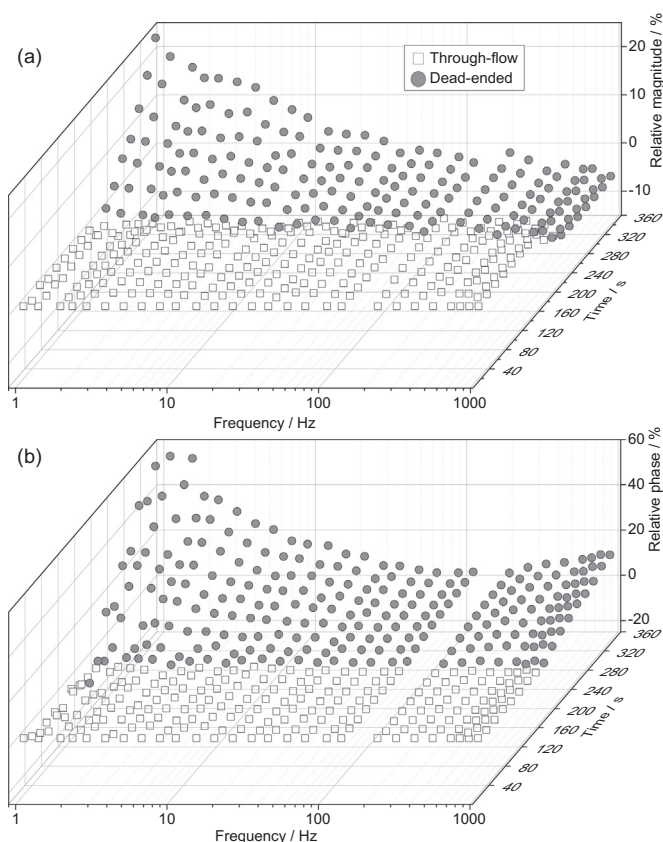

Fig. 12. Evolutions of the relative magnitude (a) and relative phase (b) with time and frequency in through-flow and dead-ended operation.

$$\text{Relative phase}(t) = \frac{\text{Phase}(t) - \text{Phase}(0)}{\text{Phase}(0)} \quad (3)$$

The magnitude analysis (Fig. 12(a)) shows a 5% drop of resistance in the high frequency region due to the increased hydration, and a gradual increase in the low frequency region over time, reaching a 20% increase at 1 Hz and 180 s in dead-ended operation; an indication of a gradual flooding of the cell as the valve is kept closed.

In the high frequency region, the phase (Fig. 12(b)) increases over time in dead-ended mode, reaching a 15% increase at 180 s (1 kHz). This is attributed to nitrogen cross-over affecting the anode kinetics. Finally, the phase is seen to increase most markedly in the low frequency region: this is an indication of electrode flooding introducing a mass transport limitation.

4. Conclusion

Anode dead-ended/purge processes have been investigated using a combination of voltage transients, EIS, off-gas analysis and thermal imaging. The reconstructed impedance technique, performed for the first time in this paper, proved useful in determining the evolution of the Nyquist, phase and magnitude under dynamic operation.

The combination of techniques suggests that the following occurs during cycling: upon entering dead-ended operation the increase in anode pressure leads to an initial increase in performance (voltage) due to Nernstian considerations and improved hydration of the electrolyte; a combination of N$_2$ crossover and electrode flooding then leads to voltage drop that is immediately recoverable upon opening of the purge valve.

Improved understanding of the dead-ended/purge process provides a rationale for optimising the use of the technique in terms of cycle frequency and duration of the respective modes. Given the identified sources of voltage degradation, the current density, temperature, anode and cathode pressure, nature and thickness of the membrane will all influence performance.

Note that the increasing temperature observed could be an indicator of increased current density in parts of the cell. Imbalance in current distribution and temperature within the cell is expected to occur and is the subject of further work using a segmented current collector plate (S++ Simulation Services, Germany) to investigate the evolution of these localised variables compared to the global evolution studied in the present work.

References

[1] P. Moçotéguy, F. Druart, Y. Bultel, S. Besse, A. Rakotondrainibe, J. Power Sources 167 (2007) 349.
[2] J. Chen, J.B. Siegel, A.G. Stefanopoulou, J.R. Waldecker, Int. J. Hydrogen Energy 38 (2013) 5092.
[3] J.B. Siegel, S.V. Bohac, A.G. Stefanopoulou, S. Yesilyurt, J. Electrochem. Soc. 157 (2010) B1081.
[4] S. Yesilyurt, J.B. Siegel, A.G. Stefanopoulou, J. Fuel Cell Sci. Technol. 9 (2012) 021012-1.
[5] A.P. Sasmito, A.S. Mujumdar, Int. J. Hydrogen Energy 36 (2011) 10917.
[6] Y. Hou, C. Shen, Z. Yang, Y. He, Renew. Energy 44 (2012) 246.

[7] A. Rabbani, M. Rokni, Appl. Energy 111 (2013) 1061.
[8] E. Muller, F. Kolb, L. Guzzella, A.G. Stefanopoulou, D. McKay, J. Fuel Cell Sci. Technol. 7 (2010) 021013-1.
[9] J. Yu, Z. Jiang, M. Hou, D. Liang, Y. Xiao, M. Dou, Z. Shao, B. Yi, J. Power Sources 246 (2014) 90.
[10] K.D. Baik, M.S. Kim, Int. J. Hydrogen Energy 36 (2011) 732.
[11] J.B. Siegel, D.A. McKay, A.G. Stefanopoulou, D.S. Hussey, D.L. Jacobson, J. Electrochem. Soc. 155 (2008) B1168.
[12] Q. Yan, H. Toghiani, J. Wu, J. Power Sources 158 (2006) 316.
[13] T. Matsuura, J. Chen, J.B. Siegel, A.G. Stefanopoulou, Int. J. Hydrogen Energy 38 (2013) 11346.
[14] J. Chen, J.B. Siegel, T. Matsuura, A.G. Stefanopoulou, J. Electrochem. Soc. 158 (2011) B1164.
[15] A. Hakenjos, H. Muenter, U. Wittstadt, C. Hebling, J. Power Sources 131 (2004) 213.
[16] M. Wilkinson, M. Blanco, E. Gu, J.J. Martin, D.P. Wilkinson, J.J. Zhang, H. Wang, Electrochem. Solid State Lett. 9 (2006) 507.
[17] M. Matian, A. Marquis, D. Brett, N. Brandon, Proc Inst Mech Eng Part A J Power Energy 224 (2010) 1069.
[18] G. Zhang, L. Guo, L. Ma, H. Liu, J. Power Sources 195 (2010) 3597.
[19] O. Lottin, T. Colinart, S. Chupin, S. Didierjean, J. Power Sources 180 (2008) 748.
[20] M. Wang, H. Guo, C. Ma, J. Power Sources 157 (2006) 181.
[21] H. Guo, M. Hai, F. Ye, C. Fang, Int. J. Hydrogen Energy 37 (2012) 13155.
[22] L.S. Martins, J.E.F.C. Gardolinski, J.V.C. Vargas, J.C. Ordonez, S.C. Amico, M.M.C. Forte, Appl. Therm. Eng. 29 (2009) 3036.
[23] R. Shimoi, M. Masuda, K. Fushinobu, Y. Kozawa, K. Okazaki, J. Energy Resour. ASME 126 (2004) 258.
[24] M. Matian, A.J. Marquis, N.P. Brandon, Int. J. Hydrogen Energy 35 (2010) 12308.
[25] D.J.L. Brett, P. Aguiar, R. Clague, A.J. Marquis, S. Schöttl, R. Simpson, N.P. Brandon, J. Power Sources 166 (2007) 112.
[26] X. Yuan, H. Wang, J. Colinsun, J. Zhang, Int. J. Hydrogen Energy 32 (2007) 4365.
[27] M.U. Iftikhar, D. Riu, F. Druart, S. Rosini, Y. Bultel, N. Retière, J. Power Sources 160 (2006) 1170.
[28] S.M. Rezaei Niya, M. Hoorfar, J. Power Sources 240 (2013) 281.
[29] J. Kim, Y. Park, K. Kobayashi, M. Nagai, Solid State Ionics (2001) 313.
[30] H. Kuhn, B. Andreaus, A. Wokaun, G.G. Scherer, Electrochim. Acta 51 (2006) 1622.
[31] D.J.L. Brett, S. Atkins, N.P. Brandon, N. Vasileiadis, V. Vesovic, A.R. Kucernak, J. Power Sources 172 (2007) 2.
[32] D.J.L. Brett, S. Atkins, N.P. Brandon, V. Vesovic, N. Vasileiadis, A. Kucernak, Electrochem. Solid State Lett. 6 (2003) A63.
[33] J.-M. Le Canut, R.M. Abouatallah, D.A. Harrington, J. Electrochem. Soc. 153 (2006) A857.
[34] W. Mérida, D.A. Harrington, J.M. Le Canut, G. McLean, J. Power Sources 161 (2006) 264.
[35] Q. Meyer, S. Barass, O. Curnick, T. Reisch, D.J.L. Brett, J. Electrochem. Sci. Eng. 3 (2013) 107.
[36] E.A. Müller, F. Kolb, L. Guzzella, A.G. Stefanopoulou, D.A. McKay, J. Fuel Cell Sci. Technol. ASME 7 (2010) 021013-1.
[37] X. Yuan, J.C. Sun, M. Blanco, H. Wang, J. Zhang, D.P. Wilkinson, J. Power Sources 161 (2006) 920.
[38] X. Yan, M. Hou, L. Sun, D. Liang, Q. Shen, H. Xu, P. Ming, B. Yi, Int. J. Hydrogen Energy 32 (2007) 4358.
[39] Y. Tang, J. Zhang, C. Song, H. Liu, J. Zhang, H. Wang, S. Mackinnon, T. Peckham, J. Li, S. McDermid, P. Kozak, J. Electrochem. Soc. 153 (2006) A2036.
[40] A. Sadkowski, M. Dolata, J.-P. Diard, J. Electrochem. Soc. 151 (2004) E20.
[41] B.A. Boukamp, Solid State Ionics 62 (1993) 131.
[42] M. Urquidi-macdonald, S. Real, D.D. Macdonald, J. Electrochem. Soc. 13 (1986) 2018.
[43] M.E. Orazem, B. Tribollet, Electrochemical Impedance Spectroscopy, Wiley, New Jersey, 2008, pp. 427–445.
[44] Ramanathan, <http://www.che.iitm.ac.in/~srinivar/Software.html>, (accessed 11.05.13).